An Experimentally Validated Hyper-Viscoelastic Model for the Bending Responses of Pre-Impregnated Tapes Under Processing Conditions

QINGXUAN WEI, YAO SUN, DIANYUN ZHANG* and RYAN ENOS

ABSTRACT

Compaction of pre-impregnated fiber sheets (prepregs) is crucial to the formation of defects such as wrinkles and void. This study presents an anisotropic hyperviscoelastic constitutive model to predict the compaction deformation and force of prepregs considering the influence of temperature on resin behaviors. The entire stack of individual prepregs is homogenized as an anisotropic continuous material whose strain energy density function is developed considering normal, shear, and coupling between normal behaviors. The proposed constitutive model integrates prepreg relaxation responses through generalized Maxwell models. The proposed novel constitutive model was implemented in the commercial Finite Element Analysis (FEA) software Abaqus as a user-defined material subroutine, UMAT. The modeling parameters were characterized by a discrete micromechanics model. The modeling approach was further applied to simulate a stepwise compaction process of carbon fiber/polyamide 6 prepregs to demonstrate the predictive capability.

Qingxuan Wei, Purdue University, 610 Purdue Mall, West Lafayette, IN 47907, U.S.A. Yao Sun, Purdue University, 610 Purdue Mall, West Lafayette, IN 47907, U.S.A. Dianyun Zhang, Purdue University, 610 Purdue Mall, West Lafayette, IN 47907, U.S.A. Ryan Enos, Purdue University, 610 Purdue Mall, West Lafayette, IN 47907, U.S.A. *Corresponding Author: Dianyun Zhang—dianyun@purdue.edu

INTRODUCTION

Advanced fiber reinforced composites have boosted the transportation and high-end aerospace fields owing to their prominent durability, resistance to corrosion, design flexibility and stiffness-to-weight ratio over the past decades. Pre-impregnated fiber sheets (prepregs) play a critical role in the manufacturing of composites, providing consistent uniform resin distribution, enhanced mechanical properties and improved handling characteristics. These advantages contribute to their widespread application in various manufacturing techniques such as autoclave processing, stamp forming, and the rapidly developing automated fiber placement (AFP). Consolidation is an essential step of manufacturing, where prepregs are compacted by pressure rollers, vacuum bags, or heated platens that apply controlled pressure and heat to consolidate to ensure good bonding between plies and eliminate voids or air entrapment. It has been pointed out that the thickness change during consolidation is closely associated with void content [5, 6] and wrinkle formation at radius and tapered geometries [7, 8, 11]. Therefore, studying the compaction behavior is essential to reduce the defects and achieve consistent high-quality products. Temperature is a key factor to be considered because it greatly affects the resin status, which can be solid, liquid, and rubbery state. Take thermoplastic resin as an example. As temperature surpasses T_q , amorphous polymer transitions from a glassy solid state to a rubbery state. The reduced stiffness allows for fiber rearrangement and distinct thickness change of prepregs during compaction. If temperature exceeds melting temperature T_m , the crystalline portion also passes into soft state. Consequently, resin shows significant viscous behavior and potential flow occurs, increasing the overall compressibility. Hence, it is necessary to model the compaction behavior of prepregs when resin is in the rubbery and liquid states at elevated temperature.

In the literature, lots of experimental work has been done to study the influence of temperature on the compaction behavior of prepregs with and without preconsolidation. In Valverde's work [10], fiber-reinforced thermoplastic cruciform samples were compacted with the same pressure but different temperatures. It shows that the material is thermally stable at temperatures below T_m , and the thickness reduction of the compacted sample is significantly smaller than the reduction for temperature above T_m . As temperature increases to a level (above T_m), resin becomes fully molten. Further increasing the temperature results in minor viscosity drop with similar thickness reduction. The compaction experiments of IM6/8552 and IMA/M21 thermoset composites shows decreasing compacted thickness with temperature increasing up to 70°C, beyond which the thickness becomes insensitive to the temperature [6]. The plies expanded in the lateral direction as they were pressed in the thickness direction, which was positively related to temperature below 70°C and converges above 70°C. The expansion was found to be nonuniformly distributed and relevant to specimen dimensions. For pre-consolidated samples, the middle layers expanded more than the top and bottom layers due to the tool/ply interaction at the boundaries. The temperature-dependency of thickness and lateral expansion are attributed to two main types of flow [1, 2, 6, 9, 10]: bleeding/percolation flow, which escapes from the fiber bed without shifting it due to pressure gradient, and squeezing/shear flow, which pushes fibers along the flow direction. Bleeding flow typically happens to low viscosity liquid, while squeezing flow is more prominent in high viscosity resin. Squeezing and bleeding flow can co-exist in one material system.

Squeezing flow may also transfer to bleeding flow, and this might explain the converging lateral expansion of thermoset composite samples [6].

Scholars also put forward various modeling approaches to study the temperaturedependent compaction behavior. Belnoue et al. [1] developed a flow-compaction model to capture the strain and strain-rate dependent viscosity of thermoset material at elevated temperature. A Power law was adopted to capture the strain-rate dependence. The strain dependence was further decomposed into two terms: one considering the compaction of a homogenized material with uniform strain and the other one accounting for the composite microstructure. Bleeding flow was treated as longitudinal squeezing flow. The uniform formulation made it easy to incorporate both flow types in his model. The transition from squeezing flow to bleeding flow was considered and triggered by either the shear strain at the edges of prepregs or the normal strain in the center reaching a critical value. The model, together with transversely isotropic Neo-Hookean model for fiber, was applied to the simulation of autoclave processing to predict wrinkling of IM7/8552 prepreg produced during bagging procedure [11]. This approach was also suitable for thermoplastic materials such as PPS and PEEK under compaction and Automated Fiber Placement (AFP) [10]. The comparison between predictions and experimental results indicates that the model has excellent capability to capture the thermoplastic thickness evolution and flow modes during compaction at high temperatures (mostly above melting point). However, contrary to the fact, the model asserts that only the bleeding flow exists for thermoplastic composites compacted below melting temperature, attributed to the quickly reached compaction plateau at these temperatures [2]. An improved model removed the coupling between locking point and the transition of flow types, but the maximum lateral expansion and compaction limit were still mainly controlled by empirical artificial strains, rather than the elastic contribution of resin and fiber. Some scholars utilized temperature-dependent parameters in the homogeneous constitutive model. Large deformation was predicted, but the deformation mechanism was not investigated.

In this study, a hyper-viscoelastic constitutive model is developed to predict the compaction behavior of prepregs when resin is in liquid and rubbery states at elevated temperature. The strain energy density function (SEDF) is decomposed into the three terms for normal behaviors, three terms for shear behaviors, and a coupling term that describes the lateral expansion due to squeezing flow. A generalized Maxwell model is associated with each energy term except for axial tension to describe the timedependence. The model was implemented via finite element analysis (FEA) commercial software Abaqus user-defined material subroutine (UMAT). The modeling parameters for prepregs with resin in the rubbery state were obtained by a discrete micromechanics model, where randomly packed fibers were explicitly modeled. A fluid-structure interaction model will be developed in future work to consider the liquid resin. Compaction experiments were carried out and compared to a corresponding simulation to examine predictive capability of the proposed model. The model is innovative owing to its efficiency and incorporation of a microscale deformation mechanism when resin is at rubbery and liquid states. The rest of the paper is organized as follows. The SEDF and stresses are formulated in the "Modeling framework" section. Then, the characterizations of modeling parameters are shown in the "Characterization of modeling parameters" section. The "Model validation" section shows the comparison between a compaction experiment and simulation to validate the methodology.

MODELING FRAMEWORK

In this section, an anisotropic hyper-viscoelastic material-processing model is developed for the compaction of multi-ply prepregs considering the temperature-dependent relaxation behavior of resin and thermal expansion. The focus is to introduce a coupling term to capture the effect of squeezing flow and add the nonequilibrium stresses, due to resin viscoelastic behavior, to the total stresses based on a Maxwell model.

Thermal expansion

Even though processing temperature mostly influences viscoelastic behavior, the model also takes into account thermal effects through a thermal expansion model. This is important when resin is in the rubbery state and subjected to temperature changes, as thermal expansion can contribute significantly to the overall deformation. In the hyperelastic modeling framework, the overall deformation gradient, F, can be multiplicatively decomposed into a mechanical part, F_M , and a thermal part, F_T [12].

$$\mathbf{F} = \mathbf{F}_M \mathbf{F}_T \tag{1}$$

The thermal deformation gradient for unidirectional prepregs is related to temperature change, $T - T_{ref}$, and coefficient of thermal expansion (CTE), α_1 and α_2 (α_3) as

$$\mathbf{F}_{T} = \begin{pmatrix} 1 + \alpha_{1}(T - T_{ref}) & 0 & 0\\ 0 & 1 + \alpha_{2}(T - T_{ref}) & 0\\ 0 & 0 & 1 + \alpha_{2}(T - T_{ref}) \end{pmatrix}$$
(2)

The CTE of a lamina can be determined through the extended concentric cylinder assemblage (ECCA) model by Zhang et al. [13]. Since time-dependent resin properties are used in the model, lamina CTE could end up being time dependent as well. However, a separate viscoelastic study of the authors' group reveals that lamina's longitudinal CTE is strongly time dependent but has small magnitude, and transverse CTE shows negligible time dependence. Therefore, it is safe to assume that CTE along each direction is constant. The values are summarized in the characterization section.

Anisotropic hyper-viscoelastic model

A mesoscale unit cell (UC) of unidirectional prepreg sheets, shown in Figure 1 (a), is homogenized as a continuous transversely isotropic hyperelastic material whose SEDF, denoted as W, can be divided into two parts: an elastic part W_e and a viscous part W_v as

$$W = W_e + W_v \tag{3}$$

The fiber direction is denoted as 1, in-plane transverse direction as 2, and out-of-plane transverse direction as 3. It is assumed that prepreg deformation during consolidation processes can be decomposed into six basic modes, which are tension/compression in

the 1-, 2-, and 3-directions as well as the shear in the 1-2, 1-3, and 2-3 planes, together with a coupling term between the tension/compression behaviors along the 2- and 3-directions. The pseudo-invariants are defined to represent the large deformation as

$$I_4^{ij} = \left(A^i\right)^T \cdot \mathbf{C} \cdot A^j \tag{4}$$

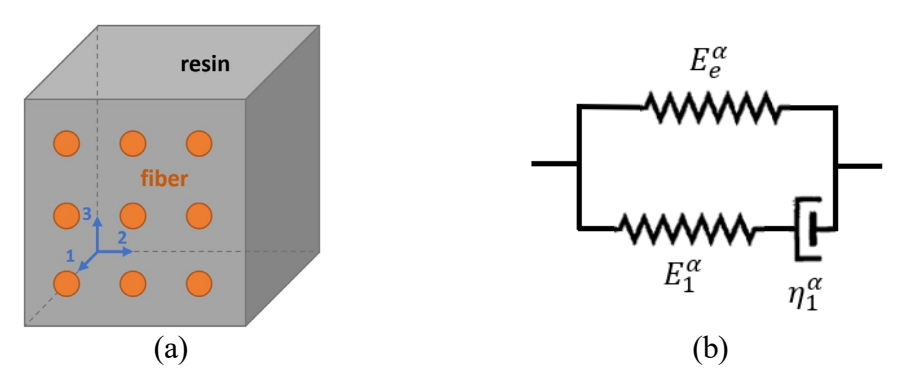


Figure 1. (a) A UC of unidirectional prepregs, and (b) The linear Maxwell model containing one elastic element and one Maxwell element.

where i and j both can be 1, 2, 3 in a three-dimensional analysis. C is the right Cauchy-Green deformation tensor computed from $C = F_M^T F_M$. The mechanical deformation gradient matrix F_M is defined as $F_M = \frac{\partial x}{\partial x}$, where x is the position in the deformed configuration and X is the position in the reference configuration. A^i are the vectors pointing in the directions of interest. Here, A^i align with the i-direction in the material coordinates. Due to the symmetry of C, there are only six independent pseudo-invariants: I_4^{11} , I_4^{22} , I_4^{33} , I_4^{12} , I_4^{13} , and I_4^{23} . Here, I_4^{11} , I_4^{22} , and I_4^{33} are the square of the stretch λ_i along each direction of interest, expressed in Equation 5. Henceforth in this paper, dummy index is ignored.

$$I_4^{ii} = \left(A^{(i)}\right)^T \cdot \mathbf{C} \cdot A^{(i)} = \lambda_i^2 \tag{5}$$

 I_4^{12}, I_4^{13} , and I_4^{23} can be related to the sinusoidal function of the shear angles γ as

$$\sin \gamma_{ij} = \frac{I_4^{ij}}{\sqrt{I_4^{ii}I_4^{jj}}} \tag{6}$$

The expression of W_e contains seven parts.

$$W^{e} = \sum_{\xi=1}^{7} W_{\xi}^{e} \tag{7}$$

The first three parts, as shown in Equation 8, describe the normal behaviors. E_1 , E_2 , and E_3 are the effective moduli controlling the fiber tension, in-plane transverse tension, and

through-thickness compaction, respectively. For a transversely isotropic material, E_2 is assumed to equal to E_3 .

$$W_i^e = \frac{E_i}{2} \left(I_4^{ii} - 1 \right)^2 \tag{8}$$

The 4th to 6th parts describe the shear behaviors and are expressed in Equation 9, where k = i + j + 1 and i < j. G_{ij} is the modulus that controls the shear behavior in i-j plane. ξ_{ij} is the initial value of $\sin \gamma_{ij}$.

$$W_k^e = \frac{G_{ij}}{2} \left(\frac{I_4^{ij}}{\sqrt{I_4^{ii} I_4^{jj}}} - \xi_{ij} \right)^2$$
 (9)

The last part describes the lateral expansion by coupling the normal behaviors along 2-and 3-directions.

$$W_7^e = D_1 (1 - J_2)^2 (10)$$

 D_1 is the modulus controlling the extent of the Poisson's effect along the 2- and 3-directions. Since fiber is inextensible in the axial direction, it is assumed that through-thickness compaction does not cause any expansion in the 1-direction. Without the coupling term W_{couple}^e , through-thickness compaction will result in pure material loss. With the coupling term, lateral expansion and material loss could exist at the same time. If volume is not conserved after compaction, the reduced volume is assumed to be the material loss caused by bleeding flow along the fiber direction. Larger D_1 makes the coupling stronger, decreasing the extent of material loss. J_2 is a pseudo-invariant that describes the deformed area in the 2-3 plane over the initial reference area, which is defined as

$$J_2 = \det \begin{pmatrix} \begin{bmatrix} I_4^{22} & I_4^{23} \\ I_4^{32} & I_4^{33} \end{bmatrix} \end{pmatrix} = I_4^{22} I_4^{33} - I_4^{23} I_4^{23}$$
 (11)

Then, the equilibrium second Piola-Kirchhoff stress can be computed as

$$\mathbf{S}^{\xi} = 2 \frac{\partial W_{\xi}^{e}}{\partial \mathbf{C}}, \qquad \xi = 1, 2, 3, \dots 7$$
 (12)

here ξ represents the deformation mode.

In this paper, the viscous energy was considered for all the energy terms except for W_1^e , because the axial behavior of prepregs is dominated by elastic fibers.

$$W^{v} = \sum_{\xi=2}^{7} W_{\xi}^{v} \tag{13}$$

The corresponding nonequilibrium stress Q^{ξ} of W_{ξ}^{v} is captured by a linear Maxwell model incorporating one elastic element and one Maxwell element, as shown in Figure 1 (b). The evolution of Q^{ξ} is described by

$$\dot{\mathbf{Q}}^{\dot{\xi}} + \frac{\mathbf{Q}^{\xi}}{\tau_{\xi}} = \dot{\mathbf{P}}^{\dot{\xi}} \tag{14}$$

where \mathbf{P}^{ξ} is the second Piola-Kirchhoff stress carried by the spring in the Maxwell arm; the relaxation time $\tau_{\xi} = \frac{\eta_{1}^{\xi}}{E_{1}^{\xi}}$; $\dot{\mathbf{Q}}^{\xi} = \frac{d\mathbf{Q}^{\xi}}{dt}$; $\dot{\mathbf{P}}^{\xi} = \frac{d\mathbf{P}^{\xi}}{dt}$; and ξ is an integer ranging from 2 to 7. Further, assume that \mathbf{P}^{ξ} is proportional to \mathbf{S}^{ξ} and the ratio is denoted as a constant β_{ξ} . It also depicts the ratio of the viscous energy to the elastic energy.

$$\frac{\mathbf{P}^{\alpha}}{\mathbf{S}^{\alpha}} = \frac{E_{1}^{\alpha}}{E_{e}^{\alpha}} = \frac{W_{\alpha}^{v}}{W_{\alpha}^{e}} = \beta_{\alpha} \tag{15}$$

Then, the evolution of Q^{ξ} can be computed by solving the ordinary differential equation.

$$\dot{\boldsymbol{Q}}^{\xi} + \frac{\boldsymbol{Q}^{\xi}}{\tau_{\xi}} = \beta_{\xi} \dot{\boldsymbol{S}}^{\alpha} \tag{16}$$

The total second Piola-Kirchhoff stress is,

$$S = \sum_{\xi=1}^{7} S^{\xi} + \sum_{\xi=2}^{7} Q^{\xi}$$
 (17)

and the total Cauchy stress is

$$\boldsymbol{\sigma} = \frac{1}{J} F \boldsymbol{S} F^T \tag{18}$$

The model was implemented in Abaqus via UMAT user-subroutine, where Cauchy stresses and the consistent Jacobian were required to be updated.

CHARACTERIZATION OF MODELING PARAMETERS

This section discusses the characterization of the modeling parameters of the hyperviscoelastic model, also referred to as the effective moduli, when resin is in the rubbery state. A discrete micromechanics model was built in Abaqus. As shown in Figure 2 (a), the model was made of a cubic representative volume element (RVE) containing randomly packed fibers in a resin domain. It is assumed that no flow is involved, and the rubbery resin has no-slip contact with fiber. The information of the RVE is displayed in Table 1. Twenty fibers [3] were included to make the cube representative enough to generate consistent homogenized properties without consuming excessive computational cost. The random packing was generated by simulating the interaction

between fibers in a periodic domain until the desired fiber volume fraction and minimum gap are achieved. In the micromechanics model, periodic boundary conditions were also applied to the faces, edges, and corners of the cube. In each model, only one homogenized stress term is non-zero, indicating free deformation for the other deformation modes. The RVE underwent a 0.01s ramp deformation process, followed by a 0.07s dwell process. Six deformation modes, i.e., axial normal (in 1-direction), transverse normal (in 2- and 3-directions), and shear (in 1-2, 1-3, and 2-3 planes), were considered separately. The total axial normal deformation was 1% of the original size, while the magnitudes of other deformation modes were 10% of the original size to consider large deformation.

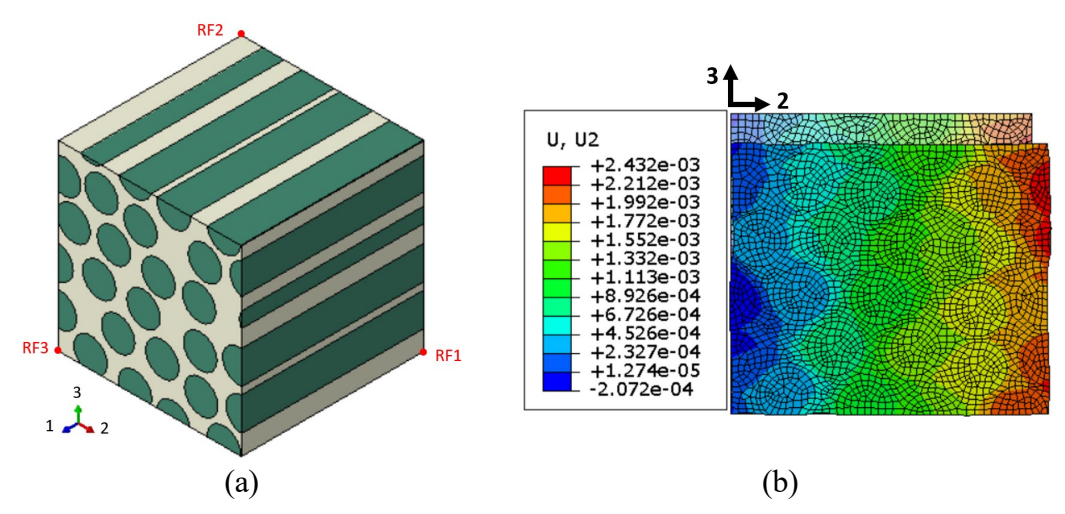


Figure 2. (a) the micromechanics model, and (b) the lateral expansion due to through-thickness compaction.

This paper investigates the behaviors of carbon fiber (CF) pre-impregnated with polyamide 6 (PA6) as an example. It has been shown in the research of Kehrer et al. [4] that the modulus of PA6 shows strong frequency dependence at 75°C, which is between PA6's glass transition temperature (50°C) and melting temperature (225°C). Therefore, 75°C is chosen as an example temperature. The storage modulus of PA6 samples with moisture content of less than 0.3wt.% was provided for temperature from 0°C to 200°C and frequency from 0.5HZ to 50HZ obtained from dynamic mechanical analysis tests [4]. The relaxation parameters of PA6 at 75°C were identified by fitting the storage modulus vs. frequency data to a linear Maxwell model in frequency domain with R-square of 95.61%, which can be expressed as

frequency domain:
$$R(\omega) = R_r + R_u \frac{\omega^2 \tau^2}{1 + \omega^2 \tau^2}$$
 (40)
time domain: $R(t) = R_r + R_u \exp\left(-\frac{t}{\tau}\right)$

where $\omega = 2\pi f$. The resulting resin parameters are shown in Table 2. Carbon fibers were modeled as a transversely isotropic linear elastic material, whose properties are also shown in Table 2.

The resulting stress of the CF/PA6 RVE was homogenized as the integration point volume average, according to Equation 41,

$$\bar{\sigma} = \sum_{i=1}^{N} \frac{V_i \sigma_i}{V} \tag{41}$$

where V_i is the volume of the *i*-th integration point, σ_i is the stress value of the *i*-th integration point, V is the total volume, and N is the total amount of integration points in the model. The stress vs. time results are shown in Figure 3, which were used to characterize the parameters of the hyper-viscoelastic model. Note that since unidirectional prepregs are transversely isotropic, σ_{22} for the normal behavior along the 2-direction and σ_{33} for the normal behavior along the 3-direction are supposed to be consistent. However, if not enough random-packed fibers were considered in the discrete RVE, large difference between σ_{22} and σ_{33} might exist. The close value of σ_{22} and σ_{33} in Figure 3 (b) suggests the validity of using 20 fibers in the current micromechanics model. The average of σ_{22} and σ_{33} was used to characterize $E_2(E_3)$, $\beta_2(\beta_3)$, and $\tau_2(\tau_3)$. Similarly, the average of σ_{12} and σ_{13} was used to characterize $G_{12}(G_{13}), \beta_4(\beta_5)$, and $\tau_4(\tau_5)$. The parameters of the coupling term were characterized by Poisson's effect in 2-3 plane. As shown in Figure 2 (b), when RVE was compacted in the 2- (or 3-) direction for 10%, expansion occurred in the 3- (or 2-) direction for 5.46% at 0.01s and 5.49% at 0.08s. The consistent expansion at 75°C indicates negligible energy dissipation for the coupling term.

TABLE 1. MODELING PARAMETERS OF THE DISCRETE MICROMECHANICS MODEL.

Parameters	Meaning	Value	Unit
l	Length of the RVE cube	3.8653E-2	mm
d	Diameter of carbon fiber	7.1E-3	mm
V_f	Fiber volume fraction	53%	-
N_f	Number of fibers	20	-
E_{1f}		231000	MPa
$E_{2f}\left(E_{3f}\right)$		15000	MPa
$v_{12f}\left(v_{13f}\right)$	Engineering constants of	0.27	
$ u_{23f}$	transversely isotropic linear elastic model	0.497	
$G_{12f}\left(G_{13f}\right)$		24000	MPa
G_{23f}		5010	MPa
R_r	Resin relaxed modulus at 75°C	867.1	MPa
R_u	Resin unrelaxed modulus at 75°C	344.4	MPa
τ	Resin relaxation time at 75°C	0.02564	S

The responses of a homogenized RVE under the same deformation modes were also modeled in Abaqus. The RVE was simply a cube of unit length, without any boundary between fiber and resin. The hyper-viscoelastic model implemented via UMAT subroutine was used in this simulation. The effective moduli of the hyper-viscoelastic model were characterized when the stress responses of the homogenized RVE agree with the stress responses of the discrete RVE. The results are also shown in Figure 3 and the characterized effective moduli are shown in Table 2.

TABLE 2. CHARACTERIZED PARAMETERS OF THE HYPER-VISCOELASTIC MODE	TABLE 2	. CHARACTERIZED	PARAMETERS (OF THE HYPER-	-VISCOELASTIC MODEI
------------------------------------------------------------------	---------	-----------------	--------------	---------------	---------------------

Parameters	Value	Unit	Parameters	Value	Unit
E_1	31000	MPa	G_{23}	825	Mpa
$E_2(E_3)$	467	Mpa	eta_6	0.36	-
$\beta_2 (\beta_3)$	0.44	-	$ au_6$	0.035	S
$ au_2(au_3)$	0.033	S	D_1	346	Mpa
$G_{12}(G_{13})$	1005	Mpa	$oldsymbol{eta_7}$	0	
$\beta_4 (\beta_5)$	0.4	-	$ au_7$	Inf	S
$ au_4(au_5)$	0.035	S	$lpha_1$	-9.000 <i>e</i> - 07	-
			$\alpha_2(\alpha_3)$	2.700e - 05	-

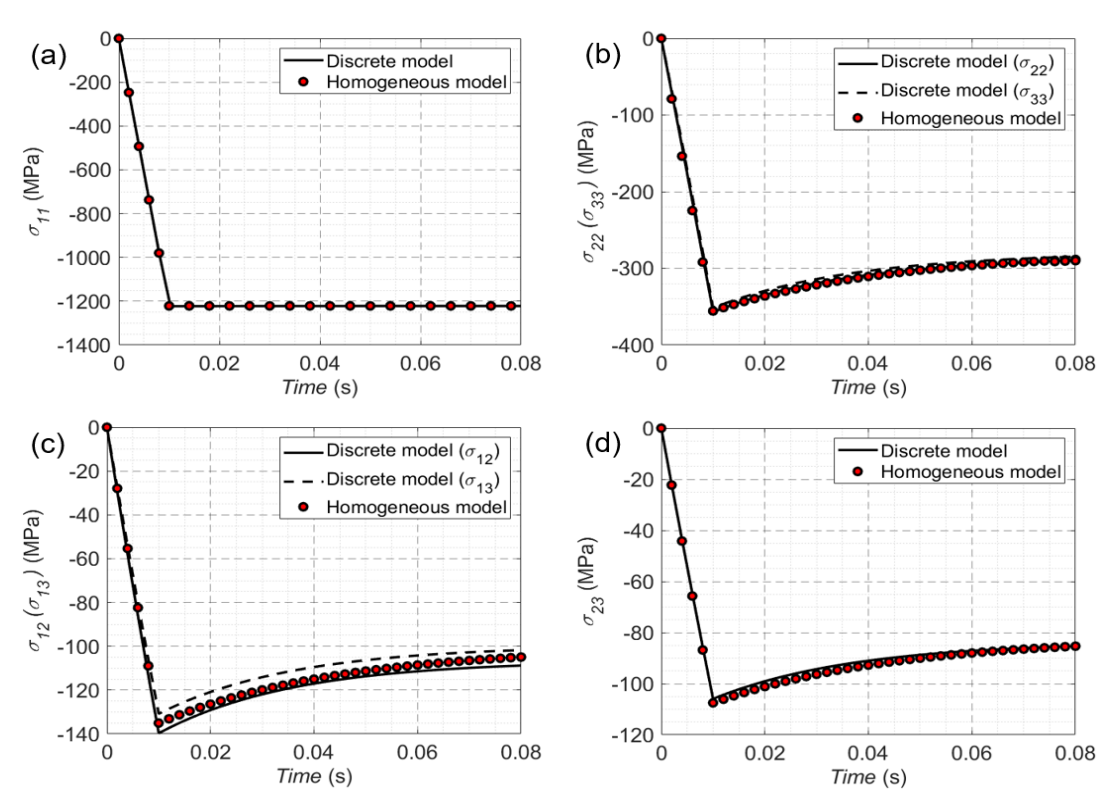


Figure 3. Consistent stresses from discrete and homogeneous models for (a) axial normal deformation, (b) transverse normal deformation, (c) shear in 1-2 and 1-3 planes, and (d) shear in 2-3 plane.

MODEL VALIDATION

To check the predictive capability of the proposed hyper-viscoelastic model, a stepwise compaction experiment was carried out and a corresponding model was implemented in Abaqus. The compaction force and deformed shape obtained from the experiments and simulations were compared.

Compaction experiment

In the compaction experiment, 65 plies of unidirectional CF/PA6 prepregs from SHINDO were compacted at 75°C in an environmental chamber. The setup of compaction tools is shown in Figure 4 (a). Two steel plates, whose surfaces that contact prepregs are 71.12 mm × 71.12 mm squares, were connected to the upper grip and lower grip of a test machine. A ruler was attached to the lower plate as a measurement reference. A camera was placed outside of the chamber to monitor the dimension change of prepregs and take pictures.

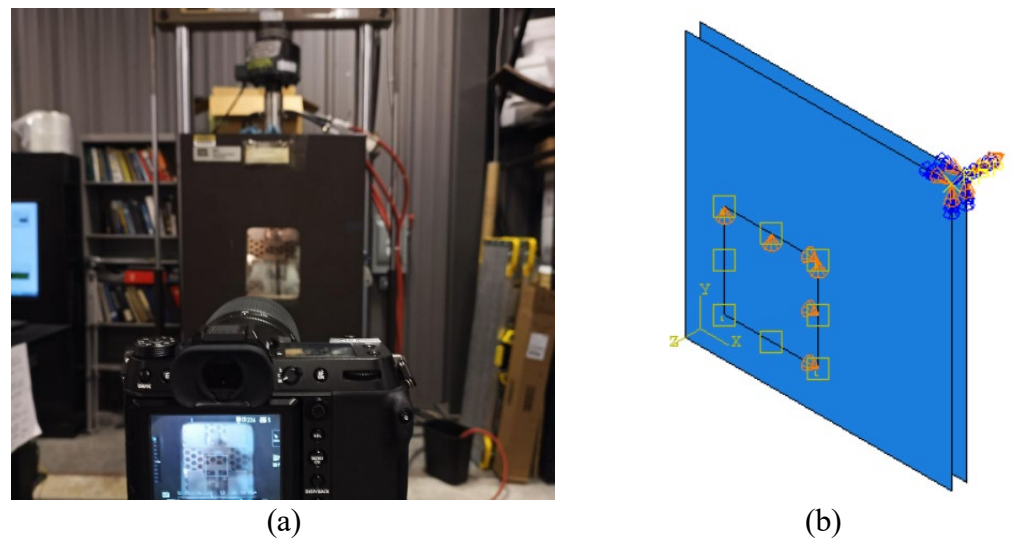


Figure 4. (a) The setup of experiments, and (b) the setup of simulation.

Before the test began, a roll of prepreg was cut into 50 mm × 50 mm square pieces, which were stacked one upon another to form a 65-layer assembly. Three assemblies were prepared to repeat the same procedure three times. Thickness was measured at three different locations for each assembly, and the average initial thickness is 4.009 mm. Then, the two compaction plates were separated by 7 mm so that a sample can be easily put in between the plates, and the whole chamber was heated from 25°C to 75°C. Then, a prepreg assembly was put in, followed by a sufficient dwell to heat the sample uniformly. Next, the distance was decreased to 4 mm as the initial status of the test, which did not affect the compaction force much. As the test started, the upper plate was fixed, and the lower plate was moved towards the upper one. The distance between the two plates was decreased at 0.15 mm/s to various distances of 3.5mm, 3mm, and

2.5mm, each of which was followed by a 4 min dwell for relaxation. Figure 5 records the history of averaged force from the three tests together with its standard deviation (sample). The force increases greatly when the tool moves. As the dwell starts, the compaction force slightly drops and then, becomes steady until the end of the dwell. Moreover, the third force increment (t = 8 min) is around four times of the second force increment (t = 4 min), which is also four times of the first increment (t = 0 min). This is because the inter-ply gap is closing when the samples is just compacted, causing small resistance to compaction. Then, the plies are nesting to achieve the applied thickness, further reducing the void content and increasing the resistance. If compaction is further enhanced, relatively soft resin is compressed more than fiber. As a result, the resin content decreases and fiber content increases along the thickness direction, and, consequently, more force is transferred through stiff fibers. Therefore, as compaction continues, the resistance of material will grow.

Figure 6 (a) and (b) show the front-view pictures of prepreg at the start and the end of the experiment. By comparing the pictures, it is clear that even though resin becomes soft at 75°C, the compaction does not lead to an evident expansion along the 2-direction. This indicates that the fiber and resin fractions along the thickness do not change a lot. The growing force increments (at t = 0, 4, 8 min) are mainly due to the closing of gaps and the nesting of prepreg layers.

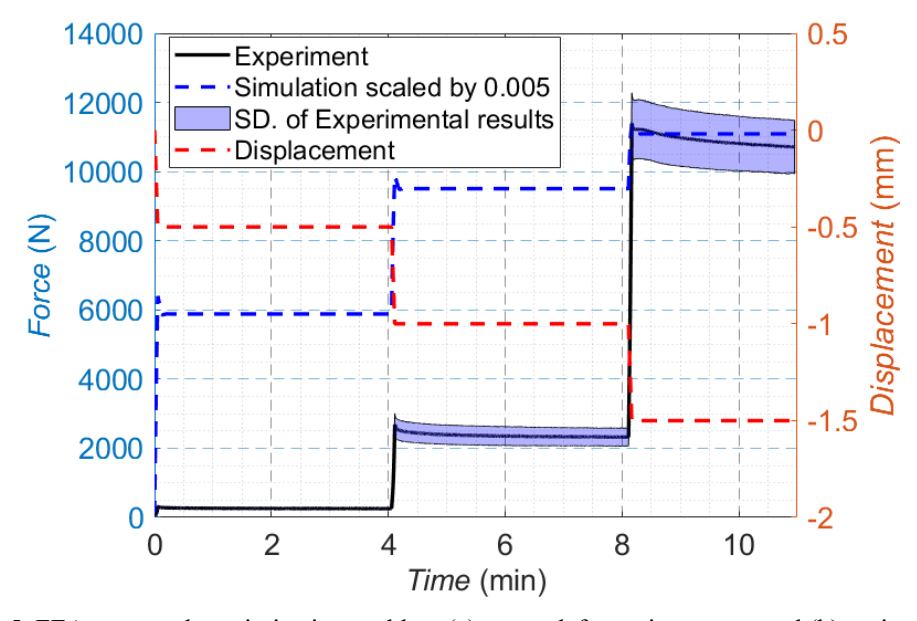


Figure 5. FEA cure-cycle optimization problem (a) stress-deformation output and (b) optimal cure-cycle compared to MRCC.

Compaction simulation

A compaction simulation was implemented in Abaqus using static, general solver for 65-layer CF/PA6 prepregs. Figure 4 (b) shows the setup of the model. In this case, global coordinates (x-y-z) are consistent with the material coordinates of the lamina (1-2-3). The top and bottom tools were created as rigid plates mastered by reference points. One of them was moved along z direction during simulation, while the other one stayed

fixed all the time. Only a quarter of the 65-layer sample was created as a 25mm x 25mm x 4mm plate, on which symmetrical boundary conditions were applied along the x- and y-directions. Initially, the prepreg plate was in contact with the fixed tool, which was 4 mm away from the other one. In the first step, only temperature increased from 25°C to 75°C, and the prepreg block expanded freely. In the second step, the moving tool moved by 0.5 mm at 0.15 mm/s towards the fixed tool, followed by a 4 min dwell. Subsequently, the motion was repeated twice, following the identical procedures, culminating in a tool separation reduction to 2.5 mm. The friction coefficient between the prepregs and tools was assumed to be a commonly adopted value of 0.3.

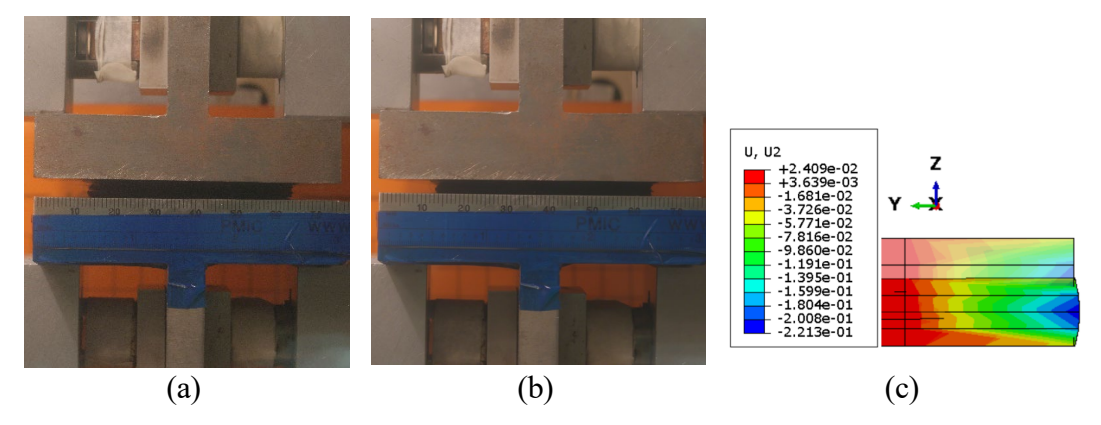


Figure 6. (a) the initial prepregs in experiments, (b) the compacted prepregs in experiments, and (c) the compacted shape in simulation.

The simulation results shown in Figure 5 record the force vs. time starting from the second step to maintain consistent procedures with the experiment. The predicted reaction force is almost 200 times of the experimental results. Also, the predicted first force increment (t=0 min) is almost twice of the second increment (t=4 min), which is also twice of the third increment (t=8 min). This is inconsistent with the trend of the experimental results. Figure 6 (b) and (c) shows that both the real expansion and predicted expansion are negligible, and the predicted lateral expansion is slightly more obvious. The inconsistency of the force might be caused by:

- 1. The experiment is conducted for multi-layer prepregs rather than thick preconsolidated prepreg laminate, while the proposed model assumes the material is continuous along the thickness and has not consider the inter-ply contact.
- 2. As compaction increases, there could be potential material loss that tends to decrease the overall resistance, but also potential increase of fiber fraction along thickness direction that tends to increase the overall compaction resistance. In the simulation, microstructure change after large compaction deformation was not considered, and material loss could be captured, leading to the "soften" of the material.
- 3. The temperature of the environmental chamber could not be precisely controlled due to the machine itself. A new environmental chamber would be used in the future.
- 4. The experiment itself could have large uncertainty due to minor sample inconsistency, human operation, etc.

FUTURE WORK

Future work will aim to consider more deformation mechanisms and improve the prediction accuracy when resin is in liquid and rubbery states:

- 1. **More deformation mechanism**. The inter-ply contact and the microstructure change after large deformation would be considered. The hyper-viscoelastic modeling parameters will be associated with microstructure parameters.
- 2. **Liquid resin**. The behavior of fibers mixed with liquid resin will be considered, including fiber's elastic contribution, resin's temperature dependent viscous behavior, and resin-fiber interaction, etc. Squeezing flow and bleeding flow will be focused on.
- 3. **Experiments**. Compaction experiments for pre-consolidated prepregs at 75 °C will be conducted and compared to the results of individual plies covered in this paper, which should reveal how much inter-ply contact contributes to the force change. More comparison between compaction experiments and simulations will be conducted at higher temperature, such as 200°C (above T_g and below T_m) and 260°C (above T_m), to check the model's predictive capability.
- 4. **Application**. The validated model will be applied to more complex process, such as stamp forming of a complex geometry and wrinkle prediction.

CONCLUSIONS

This paper puts forward a novel hyper-viscoelastic constitutive model to predict the compaction behavior of prepregs when resin in the rubbery state. The SEDF was developed considering normal, shear, and the effect of squeezing of resin. Time-dependent viscoelastic behavior is captured by generalized Maxwell models. Modeling parameters were characterized through a discrete micromechanics model. The modeling framework was applied to a compaction of CF/PA6 prepregs at 75 °C as an example. The predicted shape of compacted prepreg is generally consistent with the experimental results with slightly overpredicted lateral expansion. However, in the current study, the predicted force is larger than the experimental results with a different trend of the increasing force. The inconsistency of the compaction force was mostly attributed to the oversight of inter-ply contact and microstructure change. Future plans were made to solve the current issue and extend the model for prepregs with liquid resin.

REFERENCES

1. Belnoue JP-H, Nixon-Pearson OJ, Ivanov D, Hallett SR (2016) A novel hyper-viscoelastic model for consolidation of toughened prepregs under processing conditions. Mechanics of Materials 97:118–134. https://doi.org/10.1016/j.mechmat.2016.02.019

- 2. Belnoue JP-H, Valverde MA, Onoufriou M et al (2021) On the physical relevance of power law-based equations to describe the compaction behaviour of resin infused fibrous materials. Int J Mech Sci 199:106425. https://doi.org/10.1016/j.ijmecsci.2021.106425
- 3. D'Mello RJ, Maiarù M, Waas AM et al (2015) Modeling cure induced damage in fiber reinforced composites. 56th AIAA/ASCE/AHS/ASC Structures, Structural Dynamics, and Materials Conference. https://doi.org/10.2514/6.2015-0967
- 4. Kehrer L, Keursten J, Hirschberg V (2019) Dynamic mechanical analysis of PA 6 under hydrothermal influences and viscoelastic material modeling. Journal of Thermoplastic Composite Materials 2023:1–35. https://doi.org/10.1177/08927057231155864
- 5. Ma Y, Centea T, Nutt SR (2017) Defect reduction strategies for the manufacture of contoured laminates using vacuum BAG-only prepregs. Polym Compos 38:2016–2025. https://doi.org/10.1002/PC.23773
- 6. Nixon-Pearson O, Belnoue J-H, Ivanov D et al (2017) An experimental investigation of the consolidation behaviour of uncured prepregs under processing conditions. J Compos Mater 51:1911–1924. https://doi.org/10.1177/0021998316665681
- 7. P-H Belnoue J, Hallett SR (2020) A rapid multi-scale design tool for the prediction of wrinkle defect formation in composite components. Mater Des 187:108388. https://doi.org/10.1016/j.matdes.2019.108388
- 8. Rashidi A, Belnoue JP-H, Thompson AJ et al (2021) Consolidation-driven wrinkling in carbon/epoxy woven fabric prepregs: An experimental and numerical study. Compos Part A Appl Sci Manuf 143:106298. https://doi.org/10.1016/j.compositesa.2021.106298
- 9. Sorba G, Binetruy C, Leygue A, Comas-Cardona S (2017) Squeeze flow in heterogeneous unidirectional discontinuous viscous prepreg laminates: Experimental measurement and 3D modeling. Compos Part A Appl Sci Manuf 103:196–207. https://doi.org/10.1016/j.compositesa.2017.10.007
- 10. Valverde MA, Belnoue JP-H, Kupfer R et al (2021) Compaction behaviour of continuous fibre-reinforced thermoplastic composites under rapid processing conditions. Compos Part A Appl Sci Manuf 149:106549. https://doi.org/10.1016/j.compositesa.2021.106549
- 11. Varkonyi B, Belnoue JPH, Kratz J, Hallett SR (2020) Predicting consolidation-induced wrinkles and their effects on composites structural performance. International Journal of Material Forming 13:907–921. https://doi.org/10.1007/S12289-019-01514-2/FIGURES/12
- 12. Yosibash Z, Weiss D, Hartmann S (2014) High-order FEMs for thermohyperelasticity at finite strains. Computers and Mathematics with Applications 67:477–496. https://doi.org/10.1016/j.camwa.2013.11.003
- 13. Zhang D, Waas AM (2014) A micromechanics based multiscale model for nonlinear composites. Acta Mech 225:1391–1417. https://doi.org/10.1007/S00707-013-1057-1/METRICS